

3D Shape Analysis of the Knee Extensor and Flexor Muscles in Patients with COPD using Mesh Projection-based Features

Hengameh Mirzaalian¹, Ghassan Hamarneh¹,
Bahareh HajGhanbari², W. Darlene Reid²

¹Medical Image Analysis Lab, Simon Fraser University, BC, Canada

²Muscle Biophysics Laboratory, Vancouver Coastal Health Research Institute, Department of Physical Therapy, University of British Columbia, BC, Canada

Abstract. Loss of muscle mass in severe chronic obstructive pulmonary disease (COPD) increases the risk of mortality more than ten-fold compared to those with mild disease. Magnetic resonance imaging (MRI) has been used as a valid, reliable and non-invasive tool to investigate the changes in muscle mass in people with COPD. Using MR images to perform 3D shape analysis of thigh muscles, we extended and applied several state-of-the-art 3D shape descriptors to examine the classification accuracy of a trained support vector machine classifier to distinguish 4 thigh muscles in 20 people with COPD versus 20 healthy controls. The results of the study show high classification accuracy (with an average of 94%). Such a classification system may identify patients at risk of COPD more readily so that early interventions to reverse muscle atrophy can be provided.

1 Introduction

Chronic obstructive pulmonary disease (COPD) is defined by progressive air-flow limitation that is not fully reversible, which causes loss of thigh muscle mass (muscle atrophy) in people with COPD. The statistics reported by the World Health Organization show that COPD shares 4th and 5th places with HIV/AIDS as a single cause of death (after cardiovascular disease, cerebrovascular disease and acute respiratory infection) [4]. Magnetic resonance imaging (MRI) has been widely used as an appropriate tool for monitoring and evaluating the differences in muscle disease distribution and severity [12]. Complimentary techniques to MRI that can better detect atrophy-related changes in individual thigh muscles might facilitate targeting of interventions such as strength training and gene therapy in people with COPD [12]. Thus, more effective therapeutic approaches and preventive strategies can expedite the improvement of muscle function, exercise tolerance, and physical activity in people with COPD [12]. Such a diagnostic technique could also have more widespread application to other chronic diseases that demonstrate muscle atrophy. Recently, in [10], we investigated 3D shape and size measurements to examine the classification

accuracy of a trained support vector machine (SVM) classifier in distinguishing individual thigh muscles in a group of COPD patients compared to healthy people, whom were range-matched for age, gender, and body mass index. The aim of this study is to further explore, extend and employ state-of-the-art 3D shape descriptors (e.g. wavelet transform-based methods [14]) to achieve higher classification accuracy.

Depending on the spatial extent of the region of interest of anatomical structures, shape descriptors can be classified into two main categories: *local* or *global* features. Shape classification using local features requires establishing point correspondence between the given shapes. For neurological (non-musculoskeletal) applications, several approaches have been proposed to compare the extracted corresponding local shape descriptors for classification [21]. However, in the absence of identifiable anatomical landmarks to establish correspondence between the shapes, which is the case for thigh muscles, global shape descriptors could be more useful. Several studies have been performed to investigate the relationship between the shapes of anatomical structures and their pathological groups using global shape descriptors. For example, Durrleman et al. [6] characterized 3D shapes of brain structures via vector fields and constructed global shape descriptors by taking the integral of the vector fields. Gutman et al. [9] proposed to extract a rotation invariant shape descriptor of an inverse conformal map for the hippocampus surface using a spherical harmonics representation. Wang et al. [19] and Chen et al. [3] applied Fourier descriptors to the MR images to diagnose autism from MR images and to the description of shape changes in the human mandible, respectively.

To the best of our knowledge, there is a conspicuous scarcity of studies that have examined the relationship between (non-cardiac) muscle pathology and morphology outside our own group’s work. Kaick et al. [17] used the statistics of the Fourier coefficients extracted from 2D contours of the muscle to classify supraspinatus muscle and differentiate a normal supraspinatus muscle from several pathologies. However, these features were not used for thigh muscle classification. Ward et al. [20] computed a number of 3D shape descriptors (e.g. volume, surface area, 3D moments described in Table 1) for supraspinatus muscle classification. HajGhanbari et al. [10] used the same shape descriptors applied by Ward et al. [20] for thigh muscle classification and made them more localized by dividing each muscle into four equal quarters (regions) along its longest axis and calculated the measures for each region. In our aforementioned works, we have not yet utilized state-of-the-art 3D shape descriptors for thigh muscle classification. In Section 5, we compare the classification accuracy of our proposed method to these earlier techniques [10,20].

In this work, to study thigh muscle anatomy, we utilize a method that encodes localized morphological properties without the prerequisite of explicitly calculating a point-to-point correspondence between shapes. In particular, we first apply the wavelet transform (WT)-based shape descriptors proposed by Papadakis et al. [14] (Section 3); second, we propose a methodological extension of Papadakis et al.’s work [14] in a way that the descriptor follows the natural geometry of the

	Measurement	Description
1	3D moment J_1	Capture characteristics of the spatial distribution of the voxels that make up the muscle shape.
2	3D moment J_2	
3	3D moment J_3	
4	Mean of distances to centroid	Measure surface non-sphericity.
5	Std. dev. of distances to centroid	
6	Eigenvalue ratio λ_1/λ_2	Characterize the tubular, planar, and spherical geometry of the shape.
7	Eigenvalue ratio λ_1/λ_3	
8	Eigenvalue ratio λ_2/λ_3	
9	Surface area	Calculated as the sum of the areas of the triangular mesh of the muscle.
10	Volume	Calculated as the number of voxels inside the mesh of the muscle multiplied by the size of each voxel in mm^3 .
11	Surface area/volume	The ratio between the surface area and volume.

Table 1: Measurements taken by Ward et al. [20] for supraspinatus muscle classification.

muscle more accurately (Section 3.2). We validate the classification accuracy of the extracted features on MR images taken from the individual thigh muscles of 40 subjects (20 healthy versus 20 people with COPD) (Section 2). The results of our study show that SVM-classifier can differentiate individual thigh muscles in COPD group from those of the healthy group with an average accuracy of 94%. A comparison between the extracted feature vectors reveals that the WT-based shape descriptors outperform Ward et al.’s [20] and HajGhanbari et al.’s [10] shape descriptors for all of the four knee flexor and hip adductor muscles. In addition, the classification accuracy of our proposed extension of the WT-based descriptors is greater than that of the original method in [14] (Section 5).

2 Material

Forty subjects, twenty people with COPD and twenty healthy adults, matched for age, gender, and body mass index participated in this study. T1-weighted MR images (field of view 40 cm^2 , matrix 256×256 , 5 mm thick) were taken from each subject’s thigh from the anterior superior iliac spine to the tibial plateau, yielding 80 to 100 axial slices for each subject. Once the images were collected using the DICOM image file format, they were loaded into ITK-SNAP software [10]. Slice-by-slice segmentation of 4 individual thigh muscles was performed by an expert clinician (Figure 1). Finally, triangulated meshes were extracted from the ITK-SNAP 3D segmentation and were used for the shape representation and classification steps. Note that, in this study, in order to prepare scale and translation invariant shape descriptors, the muscles are normalized to femur length for each subject and are centered around the origin. Also, the imaging protocol ensured a consistent orientation of the knee extensor and flexor muscles

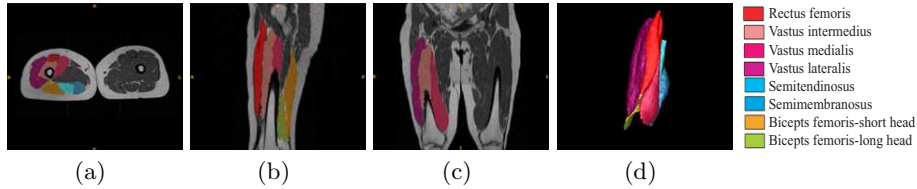


Fig. 1: Example segmentation of the knee extensor and flexor muscles in ITK-SNAP: (a) Horizontal, (b) sagittal, (c) coronal, and (d) 3D mesh view. The different knee extensors and flexors are represented by different colors.

across all subjects. More details about the data acquisition and surface mesh preparation can be found in [10].

3 2D Wavelet Transform Shape Descriptors

Papadakis et al. [14] computed 3D shape descriptors using the mean and variance of the wavelet transform (WT) coefficients of panoramic views of a 3D object. In the following sections, we illustrate how to extract the panoramic views of the 3D mesh of the muscle (Section 3.1) and then describe our proposed extensions to the cylindrical projection (Section 3.2). Finally, we discuss the extracted WT-based shape descriptors (Section 3.3).

3.1 Extraction of Panoramic Views by Cylindrical Projection

A panoramic view of a 3D object is obtained by projecting the 3D object onto the lateral surface of a *projection cylinder*; a cylinder that is parallel to one of the three principal axes (X, Y, or Z). The panoramic views are used to capture the position and orientation of the object’s surface in 3D space. Figure 2(b) depicts the discretized lateral surface of the projection cylinder parallel to the Z-axis, whereas Figure 2(e) shows a cross section of the 3D object (blue curve) and the cylinder (green circle). In the cylindrical projection step of Papadakis et al.’s method [14], each point of the cylinder (e.g. point p in Figure 2(e)) would be assigned the radius r of the cylindrical coordinate of the furthest point inside the sector containing that point (e.g. point q in the gray sector in Figure 2(e)). Then, a 2D gray-scale image is created by unfolding the cylinder, such that the image pixels and intensities correspond to the cylinder’s vertices and the radii assigned to them, respectively (Figure 2(f)). Performing similar projections onto the other cylinders parallel to the X and Y axes, results in two additional gray-scale images.

Construction of the WT-based shape descriptors from the extracted 2D images resulting from X, Y and Z cylindrical projections is described in Section 3.3. Let WT-X, WT-Y and WT-Z denote the extracted WT-based shape descriptors of the projection cylinders oriented along the X, Y, and Z-axis, respectively. Papadakis et al. [14] constructed the shape descriptors by concatenating WT-X, WT-Y and WT-Z into WT-XYZ, i.e. $WT-XYZ = [WT-X, WT-Y, WT-Z]$. Since

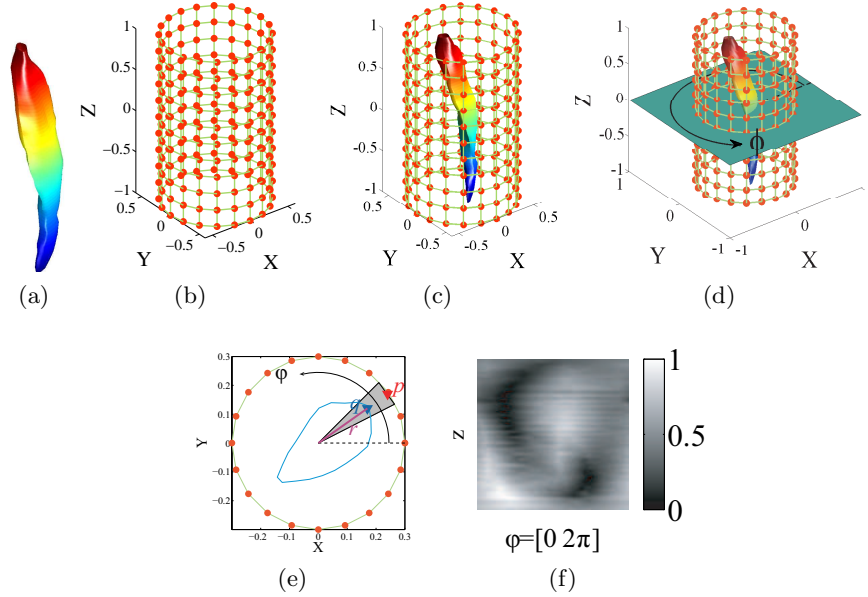


Fig. 2: Panoramic view of a 3D shape. (a) 3D mesh of a thigh muscle. The change in color from blue to red reflect the increasing Z coordinates of the mesh vertices. (b) Discretized (or sampled) cylinder, on which the muscle in (a) is projected. (c) 3D representation of both the muscle and the cylinder prior to projection. (d) 3D representation of a cross section (green plane) of the mesh and the projection cylinder. Note how the angle ϕ is defined on the plane. (e) The 2D cross section of (d). Each point on the cylinder surface (e.g. point p in (e)) is assigned the radius (r) of the cylindrical coordinate of the furthest point of the muscle (blue curve) inside the sector containing that point (e.g. point q in the gray sector). (f) 2D image obtained from unfolding the cylinder in (b). The intensity values at each pixel of the 2D image in (f) correspond to the radii r assigned to the cylinder’s vertices.

each thigh muscle in our study has a tube-like prolate shape that is elongated and aligned along the Z -axis (i.e. the Z -axis is the principle axis of each muscle as shown in Figure 2(c)), the projections along the cylinder parallel to the Z -axis are the most informative. Our results in Section 5 confirm that using only WT- Z as the shape descriptors achieves a classification accuracy similar to that of WT-XYZ but requires only about one third of the computation.

3.2 Extraction of Panoramic Views by Mesh Projections

Generally, the linear axes of the muscles are aligned with the Z -axis. However, to be more precise, each muscle has a *non-linear* (curved) axis that extends along the muscle’s central axis (or medial axes). For this reason, cylindrical projections that follow the natural curved axis of the muscle geometry are more accurate and are expected to be even more descriptive than those resulting from a linear axis. In this subsection, we describe the details of developing this curved axis extension.

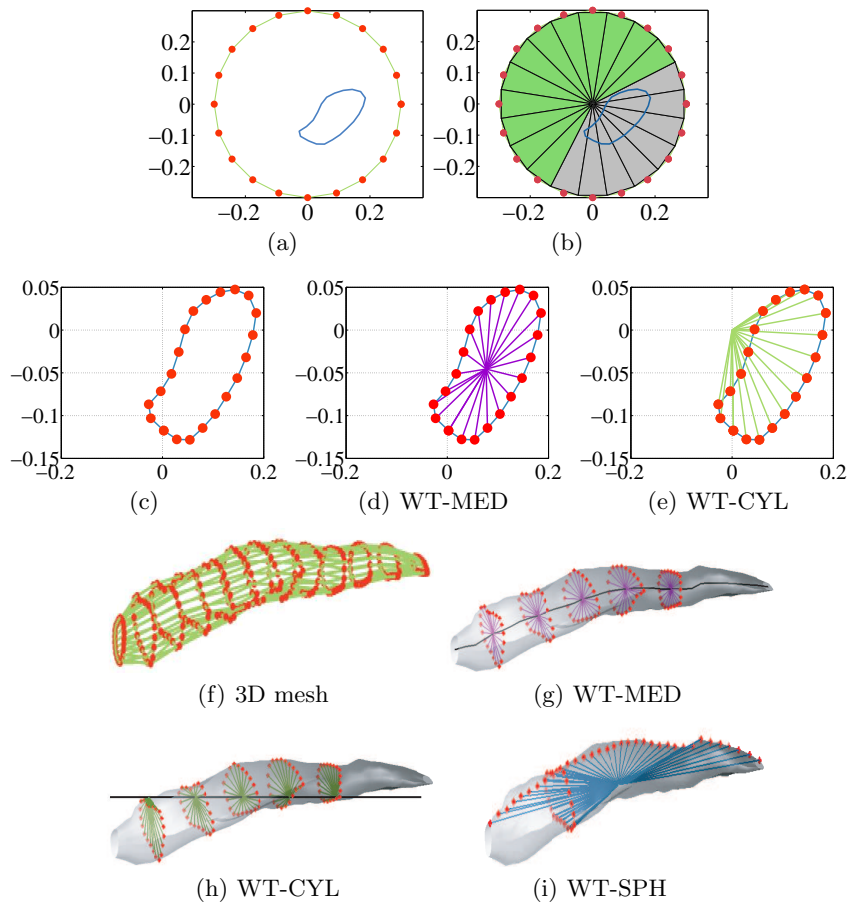


Fig. 3: Extraction of panoramic views by mesh projection. (a) Cross section of the muscle (blue curve) and the cylinder (green circle). (b) There is no intersection of the muscle (blue curve) with any of the green sectors. (c) Vertices of the contour of the mesh in the cross section. (d) Distances (purple lines) from the centroid of the curve to the mesh vertices in the cross section. (e) Radius of the cylindrical coordinate of the points (green lines), i.e. the distance from the origin $(x, y) = (0, 0)$ to the mesh vertices in the cross section. (f) 3D mesh of the muscle. (g-i) 3D representation of the distances assigned to the vertices based on: (g) the medial curve of the muscle; (h) the radius of the cylindrical; and (i) the radius of the spherical coordinates.

Our methodological extension is illustrated with the example in Figure 3. Given a cross section of the muscle (blue curve) and the Z-axis-aligned cylinder (green circle) shown in Figure 3(a), in the cylindrical projection step of Papadakis et al.'s method [14], the values assigned to the vertices belonging to the green sectors in Figure 3(b), would be zero. The reason is that none of the points of the muscle's cross-section contour (blue curve) lie inside any of those sectors.

As the primary goal is to characterize local geometrical properties, assigning zero values to the sectors that do not intersect with the muscle would cause

a problem because this results in having sectors devoid of mesh points in the projection images; and due to that, the unfolded image would contain numerous missing pixel values. Clearly, this approach would lose information that captures the muscle mesh geometry. To address this problem, we perform the projections on a curved cylinder whose axis follows the geometry (the central or medial axis) of the muscle, rather than performing the projections on the Z-axis-aligned cylinder. In other words, we effectively perform the projections onto the muscle mesh itself.

Given the 3D mesh of the muscle (Figure 3(f)), we compute the 2D projection image by first assigning values to the mesh vertices and then unfolding the mesh into the 2D image with scalar-valued pixels. The values assigned to the vertices are chosen to be the radii of the polar coordinates of the muscle cross section, with the caveat that the center of the coordinate system has to be translated from its position along the Z-axis (Figure 3(d)) into its new position at the center of the muscle cross section curve (Figure 3(e)). Collecting these new cross section centers from cross sections at different Z values form the curved axis of the muscle (black curve in Figure 3(g)); an approximation of the muscles medial axis [15,16]. Finally, we collect the WT-based shape descriptors of the resulting image into the vector WT-MED (short for wavelet-medial).

We also evaluate two additional variant approaches:

- I . In contrast to WT-MED, the first variant does not translate the center of the polar coordinate system but rather maintains its position along the Z-axis (similar to the original WT-Z). However, different from WT-Z, which assigns a value to each vertex of the projection cylinder parallel to the Z-axis, this method assigns a distance to each vertex of the muscle’s mesh (Figure 3(h)). The assigned values are effectively the radii of a cylindrical coordinate system representation. Therefore, we refer to the extracted WT-based shape descriptors from the resulting image by WT-CYL.
- II . The second variant assigns the distance from the center of the muscle in 3D (not the center of the 2D cross section of the muscle) to the mesh (Figure 3(i)). This essentially encodes the radius of the spherical coordinates of the mesh vertices and, hence, we refer to this approach as WT-SPH.

3.3 Statistics of the WT Coefficients

All of the projection approaches presented earlier result in 2D scalar images, which we denote by $f(u, v)$. The wavelet transform is then performed on these 2D images and wavelet coefficients are collected to construct the shape descriptors. Similar to the Fourier transform (or Fourier analysis or decomposition), which captures the magnitudes of different sinusoidal harmonics or frequencies existing in the whole 1D function (or signal) or 2D image, the wavelet transform achieves the same goal with the following extensions [2]. Instead of a global view of the sinusoidal frequencies that make up the whole signal, the wavelet transform focuses on analyzing the similarities between different *localized* regions of the signal and scaled and translated versions of certain function, known as the mother wavelet (instead of the sinusoidal functions in the Fourier analysis). In

particular, the discrete wavelet transform dwt coefficients of the 2D image $f(u, v)$ are extracted by:

$$dwt(s, a, b) = \frac{1}{\sqrt{s}} \sum_{u=1}^M \sum_{v=1}^N f(u, v) \psi\left(\frac{u-a}{s}, \frac{v-b}{s}\right) \quad (1)$$

where ψ is the mother wavelet, and s and (a, b) are scale and translation parameters, respectively. In the WT framework, the WT coefficients are extracted from the different subband images of f resulting from filtering and sub-sampling of f at different scales. At each scale s , there are three detail images, denoted by f_s^{LH} , f_s^{HL} and f_s^{HH} , each of which respectively contains the horizontal, vertical and diagonal high frequency information of the image. There is also an approximation image, denoted by f_s^{LL} , which contains the low frequency information (f_s^{LL} is recursively decomposed as shown in Figure 4). For N different decomposition levels, the total number of subband images f_i is $3 \times N + 1$: $f_i \in \{f_s^{LH}, f_s^{HL}, f_s^{HH}, f_s^{LL}\}$ for $s \in \{1, 2, \dots, N\}$.

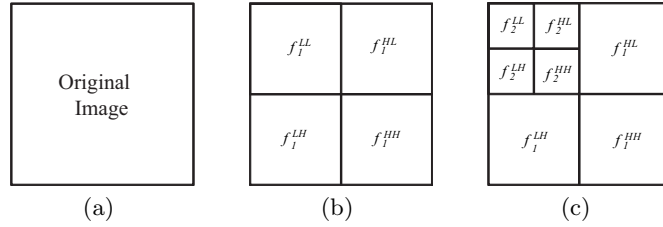


Fig. 4: Wavelet decomposition of a 2D image. A schematic diagram showing how an original image (a) is decomposed into 4 subbands (b) (i.e. one-level, $N = 1$), and then how f_1^{LL} is further decomposed (c) resulting in 7 subbands (i.e. two-level, $N = 2$).

The WT-based feature vector FV of f is computed as the concatenation of the means and variances, μ_i and σ_i , of the WT coefficients of every subband image f_i , and is given by:

$$FV = \{FV_1, FV_2, \dots, FV_{3 \times N + 1}\}, \quad FV_i = \{\mu_i, \sigma_i\}. \quad (2)$$

where μ_i and σ_i of the computed coefficients dwt_i (1) of the i^{th} subband image f_i of size $m_i \times n_i$ are given by:

$$\mu_i = \frac{\sum_{u=1}^{m_i} \sum_{v=1}^{n_i} |dwt_i(s, u, v)|}{m_i \times n_i}, \quad \sigma_i = \sqrt{\frac{\sum_{u=1}^{m_i} \sum_{v=1}^{n_i} (dwt_i(s, u, v) - \mu_i)^2}{m_i \times n_i}}. \quad (3)$$

The WT-based features in [14] (WT-XYZ) are extracted using (2) for the computed X, Y and Z panoramic views of the object (Section 3.1).

4 Muscle Shape Classification

Given a mesh representing a segmented muscle from a novel 3D medical image, our goal is to distinguish abnormal muscles from healthy muscles. In particular, we would like to perform 4 independent classification tasks for the 4 muscles: rectus femoris (RF), vastus lateralis (VL), biceps femoris-short (BS), and sartorius (SS), which belong to the muscle groups: knee extensors, knee flexors, and hip adductors (Table 2). In order to evaluate the accuracy of the classifier, we perform a leave-one-out (LOO) cross-validation [18]. We use a non-linear SVM for thigh muscle classification, which requires the setting of two parameters: C , which assigns a penalty to errors, and γ , which defines the width of a radial basis function [18]. We compute the false positive (FP) and true positive (TP) rates of the classifier for different values of C and γ in a logarithmic grid search (from 2^{-8} to 2^8) to create a receiver operating characteristic (ROC) curve. Therefore, each pair of the parameters (C_i, γ_j) would generate a point (FP_{ij}, TP_{ij}) in the graph. The ROC curve is constructed by selecting the set of optimal operating points. Point (FP_{ij}, TP_{ij}) is optimal if there is no other point (FP_{mn}, TP_{mn}) such that $FP_{mn} \leq FP_{ij}$ and $TP_{mn} \geq TP_{ij}$. We use the area under the generated ROC curves (AUC) obtained from classification involving different shape descriptors to compare their discriminatory power.

5 Results

Figure 5 and Table 2 show the ROC curves and the areas under them computed for the global shape descriptors used in [20] and [10], which we denote by GLOB1 and GLOB2, respectively (Section 1), and WT-based shape descriptors (WT-XYZ, WT-Z, WT-CYL, WT-SPH and WT-MED described in Section 3) to classify 4 individual thigh muscles into normal vs. COPD cases.

Comparing the classification accuracies reported in Table 2, we make the following observations:

- i. Averaged over all the 4 muscles (column 1 in Table 2), the highest SVM classification accuracy is obtained using WT-MED, where individual muscles in the COPD group are differentiated from those in the healthy group with an average classification accuracy of 93.69%.
- ii. WT-based shape descriptors (WT-XYZ, WT-Z, WT-CYL, WT-SPH and WT-MED) outperform GLOB1 [20] and GLOB2 [10].
- iii. The classification accuracy of the 1D WT-based descriptors (WT-Z, WT-CYL, WT-SPH and WT-MED) is greater than that of the 3D descriptor (WT-XYZ) [14]. It can be seen that, for any muscle, we can find at least one 1D shape descriptor with accuracy better than 3D.
- iv. WT-based descriptors using the proposed *mesh projection* outperform the WT-Z using the *cylindrical projection*.
- v. The last column shows our recommended shape descriptor for each muscle.

Furthermore, Tables 3-4 show the recall $R = TP/(TP + FN)$ and precision $P = TP/(TP + FP)$ resulting from the optimum setting of the parameters (C, γ)

in the SVM-classifier. The results indicate that, on average over all the 4 muscles, the maximum precision and recall are achieved by our proposed WT-MED.

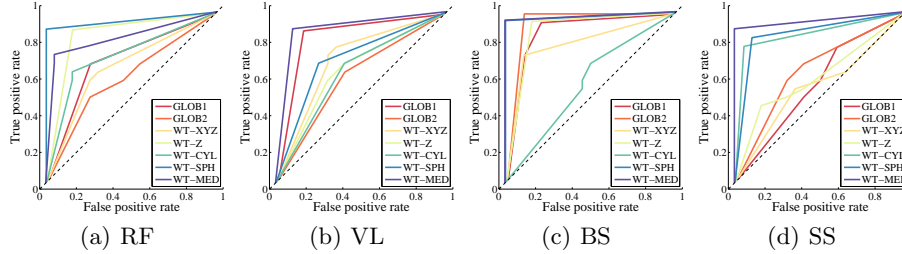


Fig. 5: ROC curves of the classifiers resulting from using the different shape descriptors for the 4 muscles. Areas under the ROC curves are reported in Table 2.

Muscle	Area under the ROC curves							Selected Descriptor(s)
	GLOB1	GLOB2	WT-XYZ	WT-Z	WT-CYL	WT-SPH	WT-MED	
RF	0.7250	0.6200	0.6837	0.8750	0.7462	0.9500	0.8475	WT-SPH
VL	0.6188	0.5938	0.7500	0.5413	0.7900	0.7250	0.9750	WT-MED
BS	0.9025	0.9500	0.8250	0.9000	0.5813	0.9750	0.9750	WT-SPH, WT-MED
SS	0.5850	0.6650	0.5650	0.6225	0.8750	0.8750	0.9500	WT-MED
Mean	0.7078	0.7072	0.7059	0.7347	0.7481	0.8812	0.9369	

Table 2: Area under the ROC curves in Figure 5. Highest accuracy acquired for each muscle is colored in red. The last column shows, for each muscle, the shape descriptor(s) that resulted in the highest AUC.

Muscle	Precision of the classifier							Selected Descriptor(s)
	GLOB1	GLOB2	WT-XYZ	WT-Z	WT-CYL	WT-SPH	WT-MED	
RF	0.7143	0.5930	0.6594	0.8947	0.6942	0.9091	0.7804	WT-SPH
VL	0.5955	0.5544	0.7500	0.5291	0.7148	0.7647	0.9524	WT-MED
BS	0.8619	1.0000	0.7826	0.9444	0.5846	0.9524	0.9524	WT-MED
SS	0.5919	0.6515	0.5455	0.5873	0.8261	0.8571	0.9091	WT-MED
Mean	0.6909	0.6997	0.6844	0.7389	0.7049	0.8708	0.8986	

Table 3: Precision values resulting from using the optimum setting of the parameters (C, γ) in SVM-classifier.

6 Discussion and Conclusion

A computer-aided method for diagnosing muscle atrophy in people with COPD could facilitate targeting of interventions such as strength training or gene therapy. In order to differentiate 4 individual thigh muscles in the healthy versus COPD groups, we first applied a state-of-the-art 3D shape descriptor; the WT-based shape descriptor proposed by Papadakis et al. [14] resulting in cylindrical projections. A comparison between the classification accuracies obtained by the

Muscle	Recall of the classifier							Selected Descriptor(s)
	GLOB1	GLOB2	WT-XYZ	WT-Z	WT-CYL	WT-SPH	WT-MED	
RF	0.7000	0.6000	0.6250	0.9000	0.6250	0.9000	0.7500	WT-SPH
VL	0.5250	0.4500	0.7500	0.4500	0.6500	0.8000	0.9500	WT-MED
BS	0.8500	1.0000	0.7500	0.9500	0.6167	0.9500	0.9500	WT-MED
SS	0.6500	0.6500	0.6000	0.5000	0.8000	0.8500	0.9000	WT-MED
Mean	0.6813	0.6750	0.6813	0.7000	0.6729	0.8750	0.8875	

Table 4: Recall values resulting from using the optimum setting of parameters (C, γ) in SVM-classifier.

aforementioned descriptors and the global shape descriptors by Ward et al. [20] and HajGhanbari et al. [10] shows that, averaged over all the 4 muscles, the WT-based shape descriptors outperformed the global shape descriptors.

We extended the WT-based descriptors by introducing medial-based mesh projections rather than the cylindrical projections, in order to follow the natural geometry of the muscle more accurately, and to rely on a 1D projection rather than 3D projections. The experimental results showed that we achieved improved classification results for all the 4 muscles using the extended descriptors. These results support the shape- and axis-specific use of shape descriptors for diseased muscles. Because different chronic diseases can have a differential impact on certain muscles or specific muscle regions, muscle-specific shape descriptors should be applied to better discriminate muscle anomalies.

Although the presented descriptors were applied to differentiate thigh muscles, they might have a widespread application for other conditions and chronic diseases that result in muscle atrophy such as chronic heart diseases, AIDS, cancer, and osteoarthritis [1].

One direction for future work is to extend the medial-based, mesh-projection descriptors to complex anatomical shapes that exhibit medial branches in their skeletons (in contrast to the single medial curve that we used here for the tube-like thigh muscles). Possible future work on muscle shape analysis include establishing point correspondence between meshes and building statistical shape models [5], examining alternative shape representation via harmonic analysis [8,13], and studying shape spaces on non-linear manifolds [11,7].

Acknowledgements

We would like to thank Oliver Van Kaick at Simon Fraser University for contributing his classification code.

References

1. J. Argiles, S. Busquets, A. Felipe, and F. Lopez-Soriano. Muscle wasting in cancer and ageing: cachexia versus sarcopenia. *Adv Gerontol*, 18:39–54, 2006. 11
2. S. A. Broughton and K. M. Bryan. *Discrete Fourier Analysis and Wavelets: Applications to Signal and Image Processing*. Wiley-Interscience, 2008. 7

3. S. Chen, P. Lestrel, W. Kerr, and J. McColl. Describing shape changes in the human mandible using elliptical Fourier functions. *Europ. J. of Orthodontics*, 3:205–216, 2000. [2](#)
4. C. Clark, L. Cochrane, E. Mackay, and B. Paton. Skeletal muscle strength and endurance in patients with mild COPD and the effects of weight training. *Eur Respir J*, 15(1):92–97, 2000. [1](#)
5. R. Davies, C. Twining, T. Cootes, and C. Taylor. Building 3D statistical shape models by direct optimization. *IEEE TMI*, 29(4):961–981, 2010. [11](#)
6. S. Durrleman, X. Pennec, A. Trounev, and N. Ayache. Statistical models of sets of curves and surfaces based on currents. *Medical Image Analysis*, 13(5):793–808, 2009. [2](#)
7. P. Fletcher, C. Lu, S. Pizer, and S. Joshi. Principal geodesic analysis for the study of nonlinear statistics of shape. *IEEE TMI*, 23(8):995–1005, 2004. [11](#)
8. G. Gerig, M. Styner, D. Jones, D. Weinberger, and J. Lieberman. Shape analysis of brain ventricles using SPHARM. 1:171–178, 2001. [11](#)
9. B. Gutman, Y. Wang, L. Ming Lui, T. E. Chan, and P. M. Thompson. Hippocampal surface analysis using spherical harmonic function applied to surface conformal mapping. *IEEE ICPR*, 3:964–967, 2006. [2](#)
10. B. HajGhanbari, G. Hamarneh, N. Changizi, A. Ward, and W. D. Reid. MRI-based 3D shape analysis of thigh muscles: Patients with chronic obstructive pulmonary disease versus healthy adults. *Academic Radiology*, 18(2):155–166, 2011. [1](#), [2](#), [3](#), [4](#), [9](#), [11](#)
11. S. Kurtek, E. Klassen, Z. Ding, and A. Srivastava. A novel riemannian framework for shape analysis of 3D objects. *IEEE CVPR*, pages 1625–1632, 2010. [11](#)
12. S. Mathur, K. Takai, D. MacIntyre, and D. Reid. Estimation of thigh muscle mass with magnetic resonance imaging in older adults and people with COPD. *American Physical Therapy*, 88:219–230, 2008. [1](#)
13. D. Nain, S. Haker, A. Bobick, and A. Tannenbaum. Multiscale 3D shape analysis using spherical wavelets. *MICCAI*, pages 459–467, 2005. [11](#)
14. P. Papadakis, I. Pratikakis, T. Theoharis, and S. Perantonis. PANORAMA: A 3D shape descriptor based on panoramic views for unsupervised 3D object retrieval. *IJCV*, 89:177–192, 2010. [2](#), [3](#), [4](#), [6](#), [8](#), [9](#), [10](#)
15. S. M. Pizer. Guest editorial-medial and medical: A good match for image analysis. *IJCV*, 55(2):79–84, 2003. [7](#)
16. K. Siddiqi and S. Pizer. *Medial Representations: Mathematics, Algorithms and Applications*. Springer, 2007. [7](#)
17. O. V. Kaick, G. Hamarneh, A. Ward, M. Schweitzer, and R. Zhang. Learning Fourier descriptors for computer-aided diagnosis of the supraspinatus. *Academic Radiology*, 17(8):1040–1049, 2010. [2](#)
18. V. Vapnik. *Statistical Learning Theory*. Wiley, 1998. [9](#)
19. S. Wang, M. K. Chung, K. Dalton, A. Alexander, and R. Davidson. Automated diagnosis of autism using Fourier series expansion of corpus callosum boundary. *Human Brain Mapping Conf*, 1:219–230, 2007. [2](#)
20. A. Ward and G. Hamarneh. 3D shape analysis of the supraspinatus muscle: A clinical study of the relationship between shape and pathology. *Academic Radiology*, 14:1229–1241, 2007. [2](#), [3](#), [9](#), [11](#)
21. B. Yeo, P. Yu, P. Grant, B. Fischl, and P. Golland. Shape analysis with overcomplete spherical wavelets. *MICCAI*, 11:468–476, 2008. [2](#)